Multi-photon polarization dependence of SSPDs.

THESIS

submitted in partial fulfillment of the
requirements for the degree of

BACHELOR OF SCIENCE
in
PHYSICS

Author :	Jaime Sáez Mollejo
Student ID :	s1898450
Supervisor :	Michiel de Dood
2^{nd} corrector :	Jan Aarts

Leiden, The Netherlands, June 23, 2017

Multi-photon polarization dependence of SSPDs.

Jaime Sáez Mollejo

Huygens-Kamerlingh Onnes Laboratory, Leiden University
P.O. Box 9500, 2300 RA Leiden, The Netherlands

June 23, 2017

Abstract

We study superconductivity and photon detection in a NbN nanobridge of 150 nm width and 4 nm thickness. Superconductivity is observed below $T_c = 8.4K$. The measured critical current as a function of temperature shows a slow decrease up to 7.9 K and more rapid decrease between 7.9 K and 8.4K. Light counts are only observed below T = 8.4K and dark counts below 7.85K. We characterize the detector by measuring the count rate as a function of polarization and average power to explore a multi-photon polarization dependence. We find a large difference in the response curves of the detector that cannot be explained by a change in the absorption efficiency η. Unfortunately, at the moment of writing the origin of the effect is inconclusive and is at least partly caused by a shift in the position of the focused laser beam on the sample when rotating a $\lambda/2$ plate to change the polarization.

Contents

Chapter 1

Introduction.

Being able to detect single photons is one of the greatest breakthroughs in physics and technology of the last decades with many possible applications. Photomultipliers and avalanche photodiodes are the traditional way to detect single photons but present limitations in their performance. These limitations may be overcome with the development of Superconducting nanowire Single-Photon Detectors (SSPDs) first reported by Gol'tsman et al. [1] in 2001.

The advantages that SSPDs exhibit over other types of single photon detectors are: low dark count rates [2], low jitter, high detection efficiency [3] and a broad spectral range. These characteristics make SSPDs prime candidates for applications such as quantum optics [4], quantum key distribution [5], interplanetary communications [6] or cancer research [7].

SSPDs consist of a thin and narrow strip of a superconducting material cooled down below its critical temperature T_c. A bias current, I_b, comparable to the critical current, I_c, is applied to the sample, making possible the transition to the normal state after the absorption of one photon of sufficient energy. This transition happens every time that a photon is absorbed, creating a small voltage pulse that is amplified and detected as a count.

The best current understanding of the detection event in NbN SSPDs is that the absorption of a photon leads to a creation of a cloud of quasiparticles weakening the superconduction. This increases the probability for a superconducting vortex to cross the wire, which leads to the formation of a normal section of the wire. Due to Joule heating the rest of the nanowire also becomes normal and creates a measurable voltage pulse. Several alternative models have been proposed such as the hotspot model [1, 8], the diffusion-based hotspot model [9], the diffusion-based vortex model [10] and the normal-state vortex model [11]. Still more research is necessary

to extend our understanding to a wider range of energies and to have a better understanding of the detection mechanism.

First experiments in the single photon detection regime point to a position dependent internal detection efficiency [12], in addition to the well-known polarization dependent absorption [13, 14]. An open question is how this polarization dependence persists in the multi-photon regime and if this can further our understanding of the detection mechanism.

Previous tomography measurements [15, 16] were limited in accuracy by power fluctuations in the laser [17]. To resolve this issue we implemented a continuous power monitor. For optimum implementation it is necessary to use a power meter with a broad dynamical range (at least 3 orders of magnitude) and low signal to noise ratio for low powers. We also reduced the laser spot size in order to minimize heating of the sample and increase the efficiency of the detector. The reduction of the spot increases the effect of mechanical vibrations of the detector. To mitigate this problem the detector and the rest of the experimental setup were mechanically coupled.

This thesis first introduces in chapter 2 the experimental setup used, followed by a characterization of the superconducting properties of the sample in chapter 3. Chapter 4 is the main part of this report and it is built up from the foundations, what is considered experimentally a detection, aiming to explain the difference in the response of the detector for two different polarizations. Also in this chapter the role of the dark counts is studied and discussed together with the superconducting properties of the NbN.

Chapter 2

Experimental setup.

Our nanodetector consists of a deposited granular film of NbN on GaAs substrate with a bow-tie shape, as shown in Fig.2.1. The wire is approximately $4nm$ thin and $150nm$ wide. The detector is cooled down inside a pulsetube cryostat to $\sim 4.4K$ and is kept at a pressure of $\sim 10^{-7}mbar$.

The detector is illuminated with a Fianium SC400 supercontinuum pulsed laser with a repetition rate of $20MHz$ and a pulse width of $20 - 30ps$. The light is filtered by a band pass filter with a center wavelength of $500nm$ and a spectral width (FWHM) of $10nm$.

At constant temperature a bias current I_b is applied through the superconductor by means of voltage biasing. Once the bias voltage, V_b, is fixed, the power incident in the sample is changed from $\sim 20nW$ to $\sim 14\mu W$ with a $\lambda/2$ plate between two crossed polarizers (Fig. 2.2). The bias voltage V_b is swept in the range where the sample is superconducting and the count rate, CR, of the detector is measured. A second $\lambda/2$ plate is used to fix the polarization incident on the detector and a $100mm$ focal length lens focuses the beam on the sample. A beam splitter is used to deviate part of the laser beam onto a power meter (ThorLabs PM100D) to monitor the power entering in the cryostat.

Figure 2.3 shows a schematic drawing of the electronic circuit used to detect photons in the experiment. The circuit can be divided in four parts: a low pass filter (R_L and C_{LP}), a bias-T (C_{BT} and L_{BT}), an equivalent electronic circuit of the detector (yellow box) [19] and finally an amplifier. The circuit ensures that the AC noise generated by the voltage source does not reach the NbN detector and once the detector generates a pulse only the high frequency components reach the amplifier.

The resistance R_L limits the current that goes through the superconductor, and measuring the voltage over R_L allows to calculate this current.

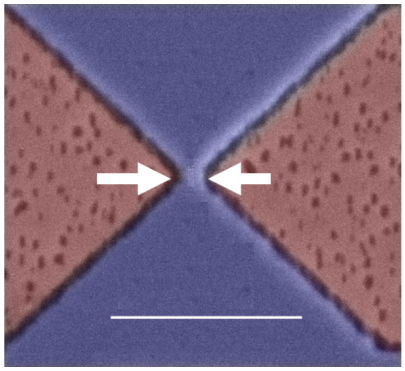

Figure 2.1: *False color SEM image of a similar detector to the one used. The blue part represent the NbN layer and the red part the GaAs substrate. The narrow bridge pointed with the arrows is the active part of the NbN. The white bar shows the distance of* $1\mu m$ *in the sample. Figure taken from [18].*

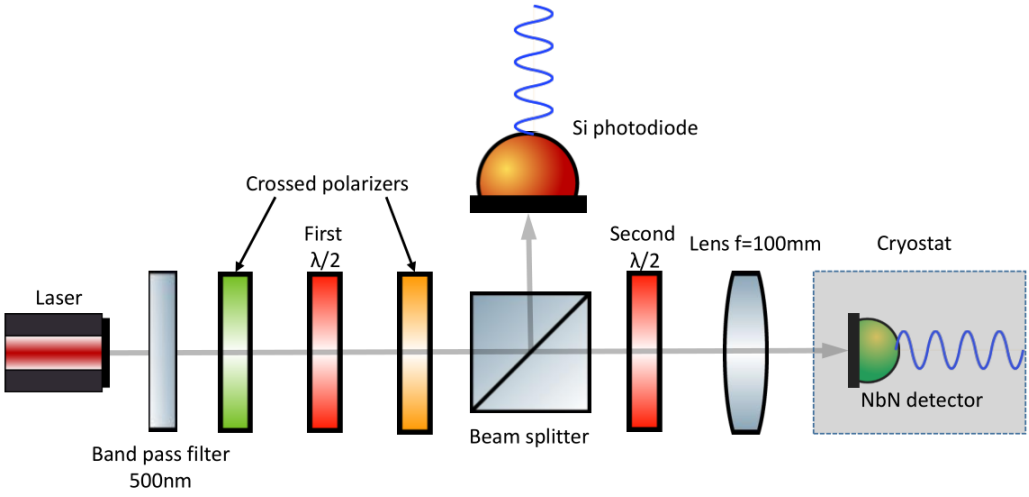

Figure 2.2: *Optical setup used to characterize the detector. The two crossed polarizers and the* $\lambda/2$ *plate regulate the transmission as* $T(\theta) \propto \cos^2(2\theta)$*. A beam splitter allows to monitor the power at all times. The second* $\lambda/2$ *plate changes the polarization of light and after this is focused on the detector with a* $100mm$ *focal length lens.*

The next two capacitors and the inductance L_{BT} ensure that all the high frequency components are filtered from the DC bias before reaching the detector. The superconductor model is characterized by a kinetic-inductance L_K and two possible states. The switch is closed for the superconducting state ($R_{superconductor} = R_{SC} \approx 0\Omega$) and open for the normal state ($R = R_N$). Every time that there is a change from switch closed to switch opened a voltage pulse is generated. Because $R_L \ll R_N$, the bias source switches from current bias to voltage bias, greatly reducing Joule heating to allow the detector to self-reset to the superconducting state. The voltage pulse is high pass filtered by C_{BT} and a 50Ω resistor, amplified and sent to a counter (not shown in Fig.2.3).

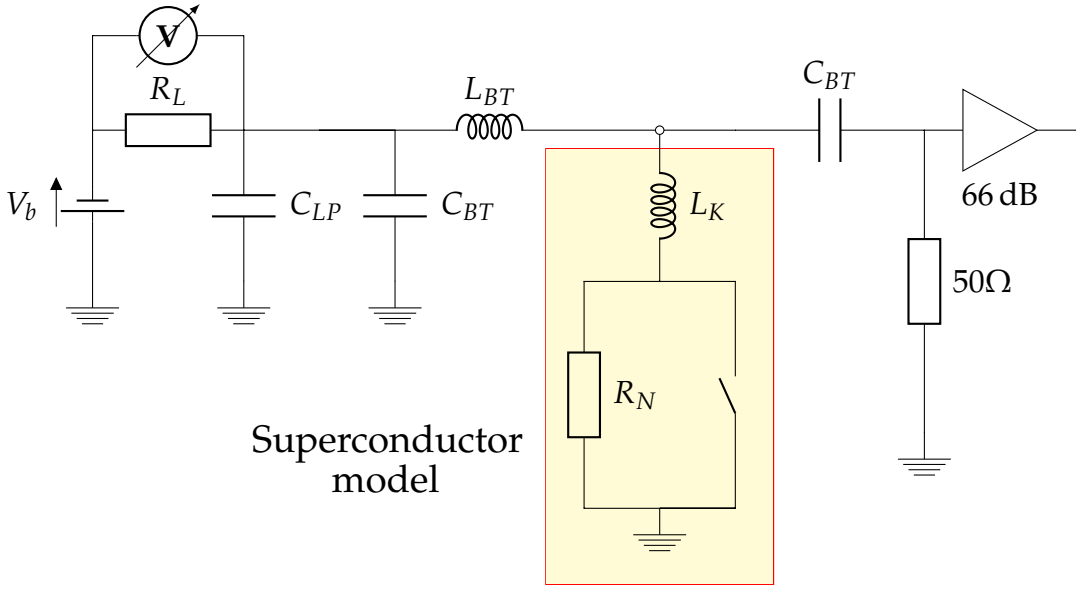

Figure 2.3: *Schematic drawing of the electrical components used to measure the voltage pulses of an SSPD. The main elements are (left to right): a voltage source followed by a low pass filter, a bias-T connected to the detector, the detector (yellow box) and an amplifier.*

Chapter 3

Superconducting properties of the detector.

3.1 Critical temperature, T_c.

Figure 3.1 presents the measured resistance of the NbN detector as a function of temperature from $260K$ to $4.1K$. This 2-wire measurement was done with a $6\frac{1}{2}$-digit multimeter (Keithley 2000) in the $1M\Omega$ regime which applies a test current of $10\mu A$.

As can be seen in the figure, the resistance increases with decreasing temperature until $20K$. Below $20K$ the resistance decreases with temperature and below $10K$ the resistance drops sharply to values $R < 1k\Omega$. At this point, it becomes difficult to measure accurately with the 2-wire measurement.

The NbN sample clearly presents a superconductor transition behavior and therefore we aim to estimate the critical temperature, T_c. As a criterion for finding T_c and the width of the transition ΔT_c, we use a linear fit (see line in Fig. 3.1) between the points that represent the 3% and 50% of the maximum resistance. From the fit we obtain a slope $(2.09 \pm 0.09)M\Omega/K$. As a result, it takes $\sim 0.3K$ to go from 3% to 50% of the normal state resistance. Taking T_c as the temperature that corresponds to the 25% of the maximum resistance, we estimate $T_c = 8.4 \pm 0.2K$. It is important to stress that this value of T_c is for a bias current of $10\mu A$.

Another important feature visible in Fig.3.1 is the gradual increase of the resistance as the temperature is decreased from $260K$ to $20K$. This behavior can be explained by a model of grain boundary scattering [20]. According to this model the resistance is proportional to $S^{-(L/D)}$, where S is

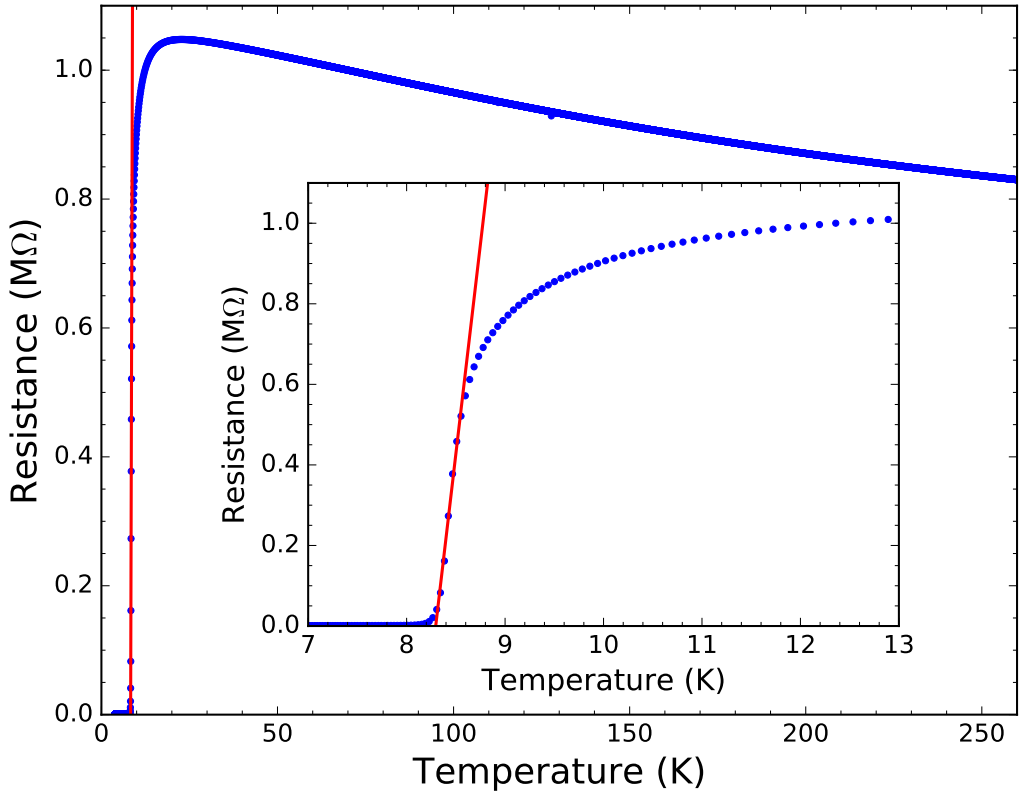

Figure 3.1: *Resistance of a NbN nanodetector as a function of temperature measured with a test current $I_b = 10\mu A$. The red line shows the slope between the points in which the resistance is between the 3% and 50% of the maximum resistance. Inset: temperature range between 7K and 13K showing the transition. The critical temperature of this NbN sample is $T_c = 8.4 \pm 0.2K$. Error bars are smaller than the symbol size.*

the probability of an electron to pass a grain boundary, L is the mean free path of the electrons and D the average grain size. Because L decreases with the temperature, the resistance increases. More details can by found in [20] and [21].

3.2 I-V curves.

To better characterize and understand the nature of the superconductivity transition in the detector, several I-V curves were measured. Figure 3.2 shows typical I-V curves at different temperatures illustrating the main features. In the experiment the bias voltage is set and the voltage over R_L is measured. From this we calculate the voltage over the superconductor, represented as R_{SC} in the inset of Fig.3.2a. All I-V curves present a steep linear part at $0mV$ and a plateau region for both positive and negative voltages. These plateaus show different characteristics depending on the temperature. From $4.1K$ to $8.05K$ the plateaus present a series of discrete decreases in the current. However, from $8.05K$ the plateau becomes continuous and almost constant. Note the decrease in the critical current of the detector as the temperature is increased.

3.2.1 Discussion.

The I-V curves in Fig.3.2 demonstrate that the NbN sample is superconducting with near-zero resistance. This conclusion is based on the almost vertical line at $0mV$ in the plots, which indicates that the sample presents zero voltage while a finite amount of current can go through. The red line represented in each plot shows the result of a linear fit, $I(V) = \frac{V}{R_0} + I_0$, taking into account all the points enclosed by the extremes of the superconducting region. From $4.1K$ to $8.60K$ the parameters of the fit are $R_0 = 7.9 \pm 0.2\Omega$ and $I_0 = -1 \pm 4\mu A$. We attribute this residual resistance to the fact that the sample is connected in series with resistive wires.

Once I_b exceeds the critical current of the sample, the I-V curves show signs of a first relaxation-oscillation regime [22]. As explained by Zhou, this is a metastable regime where the nanodetector oscillates between the normal and the superconducting states while the electronics only registers the average of the oscillating current.

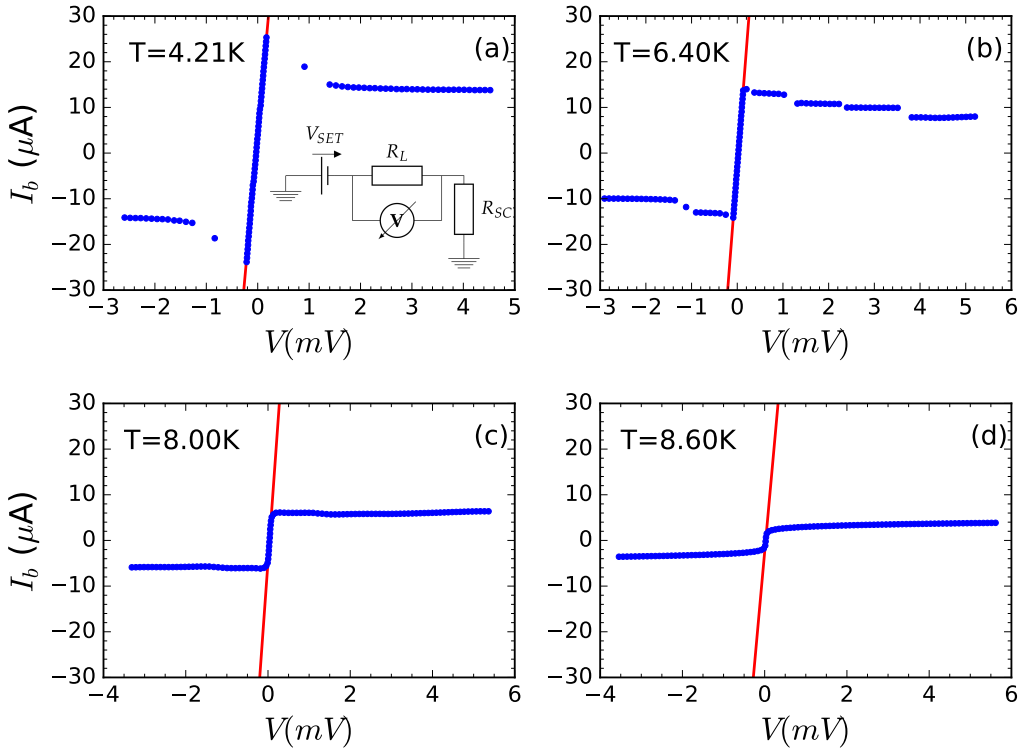

Figure 3.2: *Typical I-V curves of the NbN taken at different temperatures. The lines through the data represent a resistance of* $7.9 \pm 0.2\Omega$*. Error bars are smaller than symbols size. The inset of Fig.(a) shows a schematic circuit explaining how to obtain the voltage of the superconductor.*

3.3 I_c vs T.

As presented in Fig.3.2, the critical current of the NbN sample decreases as the temperature approaches to T_c. A more detailed study is shown in Fig.3.3 using the measured I-V curves. The critical current plotted for each temperature corresponds to the point where the slope of the I-V curve exceeds a resistance of 66Ω. As can be seen in the figure, the data presents a qualitative change in behavior at $T = 7.9 \pm 0.1K$, where the slope of the curve becomes steeper, dividing the plot in two different regions: $T \leqslant 7.9K$ and $7.9K < T < 9.1K$.

3.3.1 Discussion.

The lines in Fig.3.3 correspond to two different fits to the Ginzburg-Landau dependence $I_c(T) = I_c(0)(1 - T/T_c)^{3/2}$ in the regions mentioned before. The parameters of the dashed green fit are $I_c(T = 0) = 162 \pm 2\mu A$ and $T_c = 8.98 \pm 0.01K$, while in the case of the solid red fit are $I_c(T = 0) = 56.2 \pm 0.4\mu A$ and $T_c = 10.65 \pm 0.04K$.

The origin of this change of regime is often related to a Berezinskii-Kosterlitz-Thouless transition [23]. A detailed discussion of this transition is outside the scope of this thesis . However, this change of regime rises the question if the detector still counts above $7.9K$.

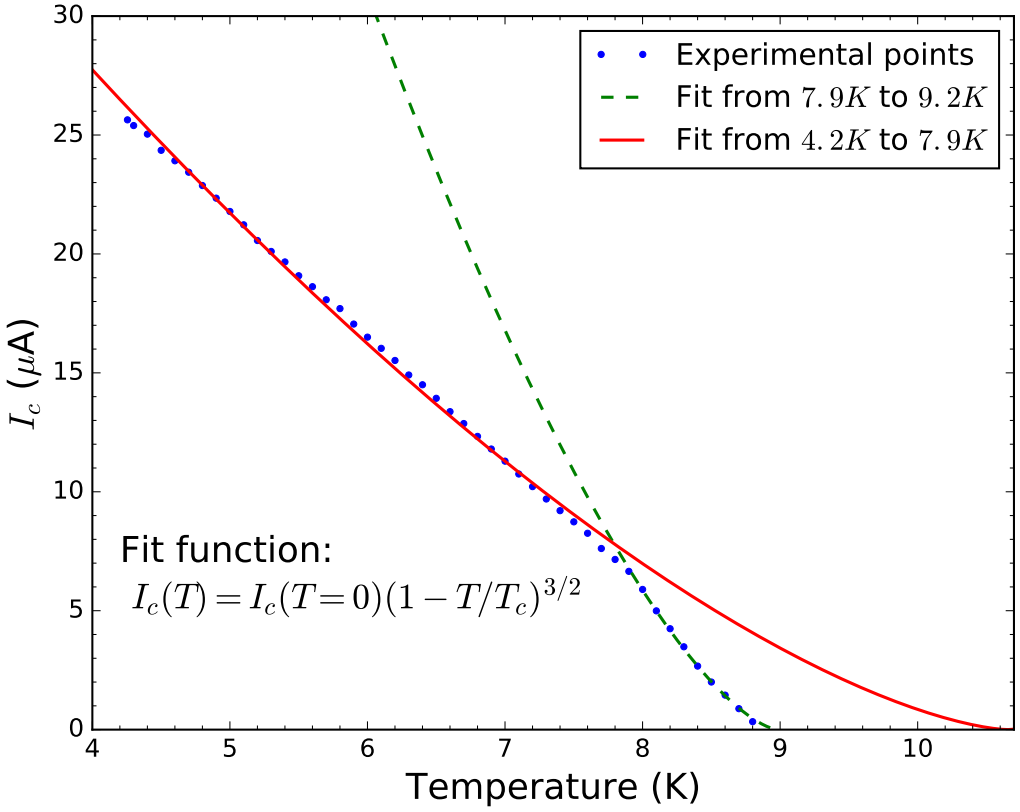

Figure 3.3: *Dependence of the critical current of the sample on the temperature. The plot presents two different regions that are fitted with the Ginzburg-Landau dependence* $I_c(T) = I_c(0)(1 - T/T_c)^{3/2}$. *The solid/red fit corresponds to the temperatures between* 4.1*K and* 7.9*K and the dashed/green fit corresponds from* 7.9*K to* 9.1*K. The parameters of the green fit are* $I_c(T = 0) = 162 \pm 2\mu A$ *and* $T_c = 8.98 \pm 0.01K$. *In the case of the red fit are* $I_c(T = 0) = 56.2 \pm 0.4\mu A$ *and* $T_c = 10.65 \pm 0.04K$. *Error bars smaller than symbol size.*

Chapter 4

Physics of the detector

We start this chapter by defining what we mean by a count and how the count rate of the detector changes when varying the bias voltage and the temperature. The correlation between the regime change in Fig.3.3 and the lack of light and dark counts above $7.9K$ is discussed. Section 4.4 addresses the polarization dependence in the multi-photon regime. We find that other factors contribute to the signal and discuss how these could be eliminated.

4.1 Pulse shape of a detection.

In this section we define what is called a detection event. As explained in the introduction, when a photon is absorbed the sample can go through a transition from the superconducting to the normal conducting state. The detection can be understood by modeling the detector using the equivalent circuit in the yellow box in Fig.2.3 [19]. The absorption of a photon breaks superconductivity and causes the sample to have a certain resistance R_n. Because $R_L \ll R_n$, the bias current I_b through the detector drops, with a time constant $\tau_{fall} = L_K/(R_n + 50\Omega)$, and causes a voltage pulse at R_L. As soon as Joule-heating, given by $R_n I(t)^2$, is sufficiently reduced, the detector cools into the superconducting regime and the I_b through the detector is recovered to its initial value, with the time constant $\tau_{rise} = L_K/50\Omega$.

Figure 4.1 shows the typical pulse shape of detection events at a temperature of $T = 4.2K$. The solid magenta and dashed blue lines correspond to the average pulse of more than 6900 pulses with bias currents of $I_b/I_c \approx 0.81$ and $I_b/I_c \approx 0.92$, respectively. The pulses plotted on top of

the average pulses correspond to a randomly chosen single pulse for each I_b/I_c ratio. The black line shows the average background noise. This background is subtracted from the pulses. The inset represents the distribution of the maximum value of each of the pulses.

These data were measured with an oscilloscope (LECROY WP7300A) capable of sampling at $3GHz$ with a trigger level of $-0.2V$. The voltage pulse was amplified by 3 identical amplifiers (Minicircuits ZX60-3018G-S+) connected in series with a broadband from $20MHz$ to $3000MHz$ and total power amplification up to $66dB$.

4.1.1 Discussion.

The shape of the pulse in Fig.4.1 shows an initial peak followed by a secondary maximum around $15-20ns$ as a result of the response of the nanodetector and the limitations of the electronics.

The pulse shape is limited by the electronics used, in particular by the low frequency cut-off of the amplifiers. The fall time τ_{fall} is limited by the sample rate of the oscilloscope and the high frequency cut-off of the amplifiers. It is not possible to register any signal faster than $0.3ns$. The rise time τ_{rise} is limited by the amplifiers, which filter the frequencies below $20MHz$. This filtering from the amplifiers explains why the average pulses become zero at the same point and the signal changes sign.

Every detection from this detector corresponds to pulses with similar characteristics to the ones shown. For the upcoming results the trigger level used for considering a count is $-0.2V$ (or $0.2V$ in case of having the inverse polarity). In our experiment there are no counts if there are no pulses with a height larger than $0.2V$.

4.2 Light and dark counts as a function of bias current.

The next step in characterizing the detector is measuring how the count rate, CR, depends on the bias current I_b.

Figure 4.2 presents the dark count rate (black symbols) and light count rate (yellow symbols) as function of applied bias current for a temperature of $4.5K$. Dark counts were measured with the detector in complete darkness covering the entrance of the cryostat with an aluminum lid. Light counts were measured illuminating the detector with a constant laser power of $\sim 10\mu W$ at a wavelength of $500nm$.

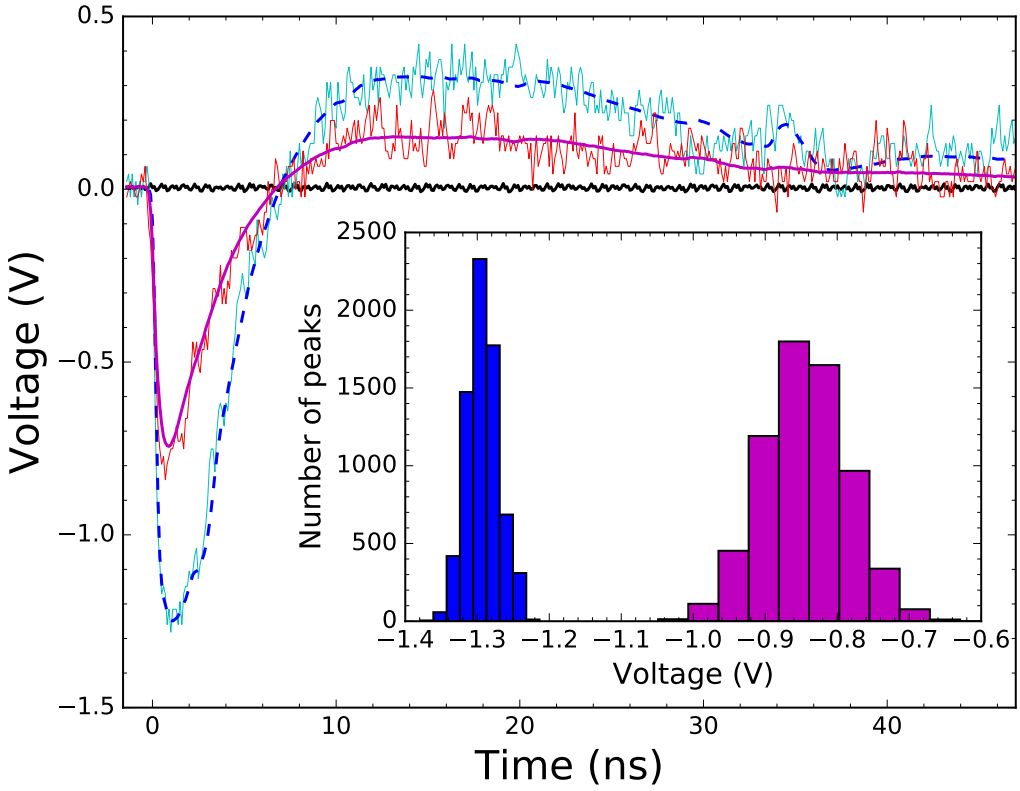

Figure 4.1: *Amplified voltage pulse at 4.2K for two different bias currents I_b. The dashed blue line represents the average pulse for $I_b/I_c \approx 0.92$ and the magenta line is the average pulse for $I_b/I_c \approx 0.81$. The curves on top of the average pulses are single pulses at the mentioned I_b/I_c ratio in each case. Inset: Distribution of the highest point of each single pulse, corresponding the colors to the same I_b/I_c ratios as before.*

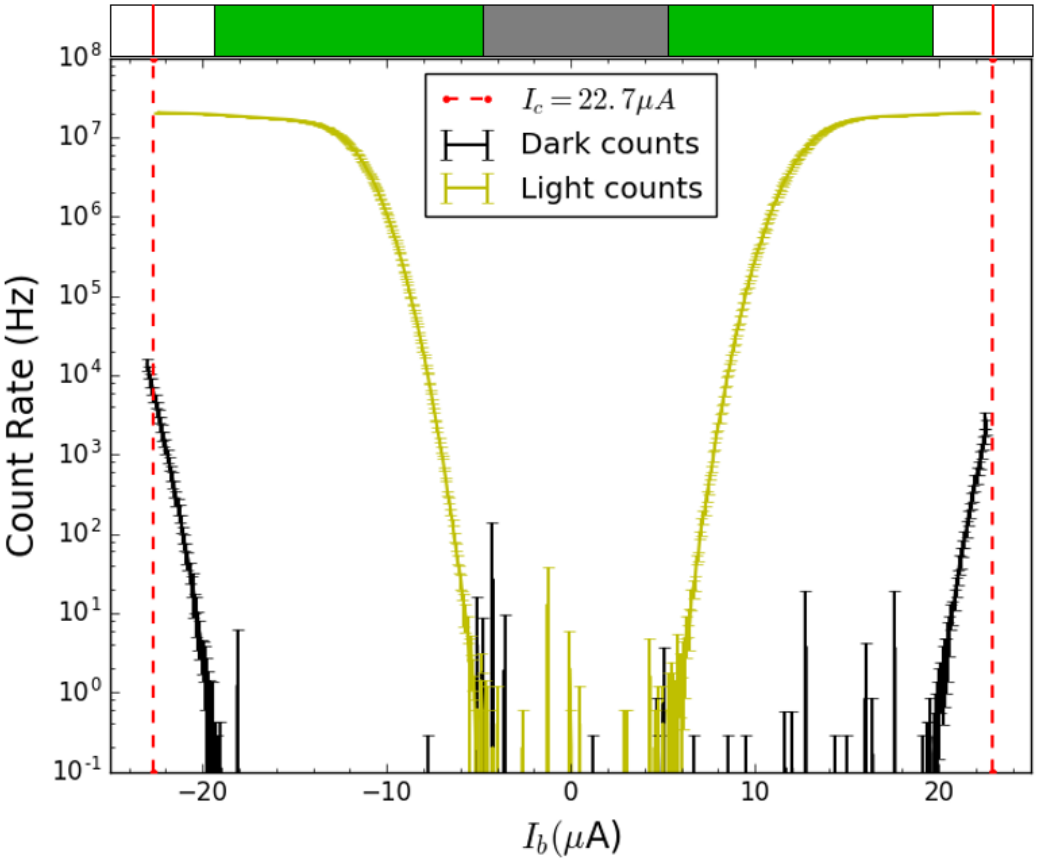

Figure 4.2: *Response of the detector at $T = 4.5K$ as function of the bias current. The dark counts present an exponential dependence on I_b. The light counts show a similar exponential behavior until $12\mu A$ where the detector starts saturating to the pulse rate of the laser illuminating with a power of $\sim 10\mu W$. The vertical dashed lines indicate the critical current of the superconductor.*

As can be seen from the figure, the light counts are present for currents exceeding $\pm 5\mu A$ and increase by 8 orders of magnitude until a count rate $\sim 2 \cdot 10^7 Hz$ is reached, a value that coincides with the pulse rate of the laser. The currents which do not present light counts are represented by the grey color in the colorbar on top of the plot. Dark counts are only measurable for currents above $\pm 20\mu A$ ($I_b / I_c = 0.87$) and show an exponential dependence on current until I_c. The colorbar shows the absence of dark counts with green and grey colors.

Above I_c, the count rates registered are of the order of 10^8, with the detector operating in the relaxation-oscillation regime. The data for $I_b > I_c$ are not presented in Fig.4.2. The white part of the colorbar above I_c presents the relaxation-oscillation regime and contains a mix of dark and light counts.

4.2.1 Discussion.

The dark counts are temporary transitions to the normal conducting state of the sample. The voltage pulse cannot be distinguished from that of light counts. The exponential regime of dark counts is consistent with the results of [24] and [23], which suggest that these fluctuations are the consequence of current-assisted thermal unbinding of vortex and anti-vortex pairs (VAP), in the context of the Berezinskii-Kosterlitz-Thouless (BKT) transition. This BKT transition is a 2D phase transition which appears at a critical temperature T_{BKT}, below the T_c of the superconductor, and happens when a characteristic dimension (e.g. width) of the superconducting sample is comparable with the coherence length of the superconductor, $\zeta(T)$. We associate the different regimes in the observed $I_C(T)$ with this BKT transition. Below T_{BKT} the vortex and anti-vortex pairs are bounded. For temperatures between T_{BKT} and T_C the vortices are free.

In the case of light counts, the results exhibit a larger sensitivity to the laser pulses for currents closer to the critical current. Moreover, the count rate measured is always at least 3 orders of magnitude larger than the dark count rate and at $T = 4.5K$ there is a wide range of I_b without dark counts (green area in the colorbar).

4.3 Role of temperature and bias voltage.

At this point there are open questions directly related to the applications of the detector, such as the sensitivity of the detector to photons, the maximum temperature at which the detector is sensitive to light or for which

temperatures and V_b the dark counts disappear. In order to understand the limitations of the detector, we need to investigate the nature of the detection mechanism and the origin of dark counts. Hence, we measured the dependence of the count rate for light counts and dark counts as a function of both bias voltage and temperature.

In this section count rate equals zero means that no counts where measured with a count rate larger than $1Hz$ and an amplified voltage pulse larger than $200mV$. The detector was illuminated with $\sim 12\mu W$.

Figure 4.3 shows a false color plot of the count rate as a function of temperature and bias voltage, using the same color code as the colorbar in Fig.4.2 (grey: zero counts for dark and light events. Green: no dark count events. White: non-zero light and dark counts). Blue circles present the critical current of the superconductor (right vertical axis), indicating the area where the sample is in the superconducting state. The solid red line and the black dashed line present the same fits as in Fig.3.3.

The grey region shows that above $8.4 \pm 0.1K$ the detector is not sensitive to any kind of detection event for the temperatures and the bias voltages measured. The green color presents a symmetric behavior considering $V_b = 0mV$ as axis and the green contour from $4.5K$ to $7.3K$ presents a linear relation for V_b and the temperature. The blue points and the green area intersect at $7.85 \pm 0.05K$ (solid black line), above this temperature there are no dark counts registered for the superconducting state, while there are counts for $V_b > 0.7mV$ and $V_b < -0.7mV$. Above $8.05 \pm 0.05K$ the sample does not present measurable dark counts for any V_b.

4.3.1 Discussion.

Figure 4.3 provides information about the process that produces the dark counts. It can be deduced that the activation of the dark count mechanism depends on temperature and V_b. At a fixed V_b between $2mV$ and $1mV$ (or $-2mV$ and $-1mV$) the count rate is zero until a temperature, where the dark count mechanism is activated. We associate this effect to the thermal excitations that produce the unbinding of the vortices [24]. The disappearance of the dark counts in the superconducting state at $7.85 \pm 0.05K$ coincides with the change of regime at $7.9 \pm 0.1K$ in Fig.3.3. These two findings need to be interpreted with caution because our research does not demonstrate a direct correlation between the lack of dark counts and the deviation of the critical current data from the Ginzburg-Landau expression for $I_c(T)$. Above $8.05 \pm 0.05K$ the count rate becomes zero for all the measured V_b, which means that the dark count mechanism is completely

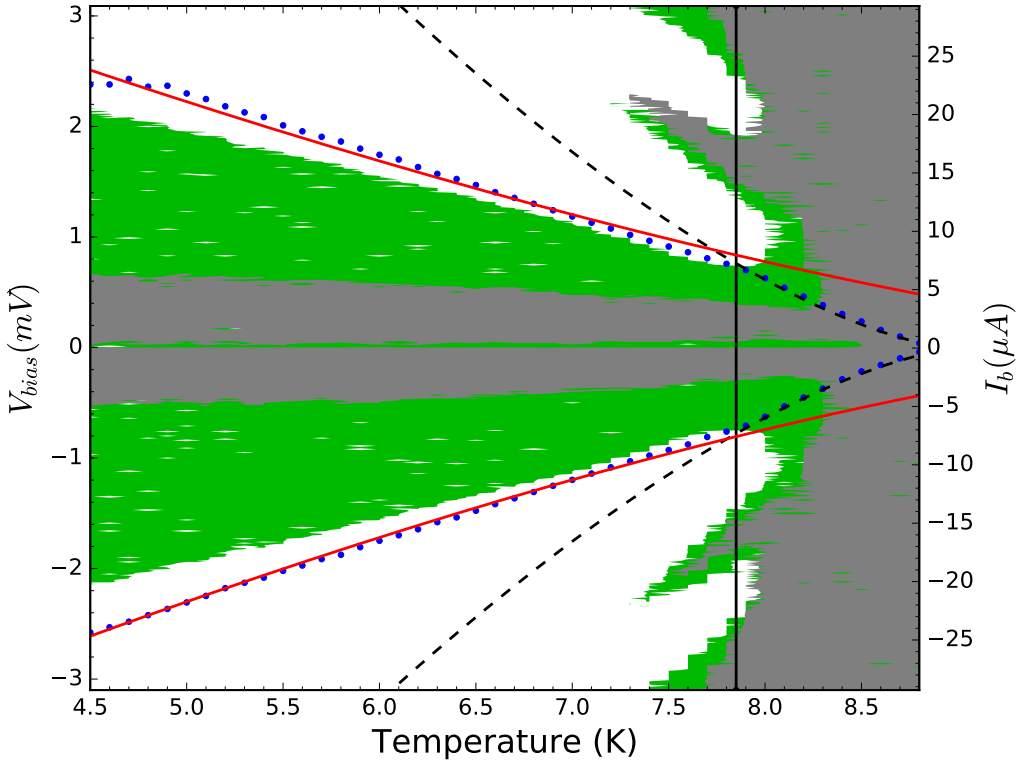

Figure 4.3: *False color plot of the count rate as function of bias voltage and temperature. Dark count rates equals to zero are observed in the grey and green area. Zero count rate for light counts is represented with grey color. The blue points represent in the right vertical axis the critical current of the superconductor, therefore the area surrounded by the points is in the superconducting state. The red solid and the black dashed lines are fits to the critical current to the Ginzburg-Landau expression* $I_c(T) = I_c(0)(1 - T/T_c)^{3/2}$.

deactivated. One possible interpretation of this result is that the nature of dark count events goes beyond the pure superconducting state.

Figure 4.3 also shows that for a fixed temperature, there is a bias voltage V_b at which the dark count events are not zero anymore. This bias voltage is close to a linear relation as a function of the temperature between $4.5K$ and $7.3K$.

The grey region shows where the detector is not sensitive when it is illuminated with $\sim 12\mu W$. The highest temperature at which the detector is sensitive to light is $8.4 \pm 0.1K$. The data shows that the detector is sensitive to photons above $7.9K$, where the change of regime of $I_c(T)$ occurs and directly answers the question of subsection 3.3.1.

The white area between the critical current and the green area presents a count rate for light counts and dark counts below or equal to the pulse rate of the laser. The white area beyond the critical current of the superconductor presents count rates larger than the pulse rate of the laser ($20MHz$), which corresponds with the relaxation-oscillation regime [22].

4.4 Polarization dependence.

4.4.1 Tomography.

In a simplified picture, the detector can click or not click when it is illuminated. The count rate is the only observable that we can measure but does not contain information about the number of photons absorbed. To understand the detection mechanism of the detector it is necessary to find a method which gives a connection between count rate and absorbed photons. Quantum detector tomography is the process which connects the two by the calculation of the Positive Operator Valued Measure [25].

Quantum detector tomography [15, 17] is used to understand the quantum response of the detector to different quantum states, in our case different Fock states or photon number states from count rate statistics using coherent states generated by the laser. Attenuating the power of the laser allows to tune the average photon number of the coherent states. Once the response of the detector to different photon distributions is measured, quantum tomography can convert this result to the response of the detector to detect a certain number of photons.

The click probability of the detector is given by:

$$R_{click}(N) = 1 - e^{-\eta N} \sum_{i=0}^{m} (1 - p_i) \frac{(\eta N)^i}{i!} \tag{4.1}$$

where N is the mean photon number of the coherent state, η is the effective absorption efficiency which describes the optical coupling and p_i is the detection probability that i absorbed photons cause a click. This expression assumes that $\eta \ll 1$ and that when the detector is saturated $p_i = 1$ for $i > m$. Also we consider $p_0 = 0$ because the click probability to detect zero photons is zero. Hence, dark counts are not considered in this equation.

One important property of equation 4.1 is the possibility to separate η and p_i [17]. This is illustrated in Fig.4.4. Figure 4.4a shows the difference between the click probability due to different η: the response has the same shapes but is shifted along the horizontal axis. Figure 4.4b presents the response for the same η but different detection probabilities p_i. In the latter case the curves present a different shape and cannot be rescaled via the effective absorption η.

The absorption presented by the NbN nanowire varies with polarization because the asymmetry of the wire imposes different boundary conditions and as a result different absorption [14]. This effect is well-understood and leads to a change in η. In addition, the detection probabilities p_i are polarization dependent, which implies that the detection mechanism itself is polarization dependent [12]. If the response of the detector for perpendicular and parallel polarization is just a difference in the absorption, both curves will have the same shape but will be shifted ($\eta_{\parallel} \neq \eta_{\perp}$ and $p_{i\parallel} = p_{i\perp}$). If the detection probabilities p_i depends on polarization, a difference in the shape of the curves must be visible ($p_{i\parallel} \neq p_{i\perp}$).

4.4.2 Experimental results.

Figure 4.5 shows the response of the polarization for perpendicular (red triangles) and parallel polarization (blue circles) for a bias current of $I_b = 20.4 \pm 0.2$ ($I_b/I_c \approx 0.87$) at $4.5K$. The horizontal axis corresponds to the average number of photons per pulse, $N = (P\lambda)/(fhc)$, where P is the power illuminating the detector, λ the wavelength of light, f the pulse rate of the laser, h Planck's constant and c the speed of light. The vertical axis is the click probability R_{Click}, which is obtained by dividing the measured count rate by the pulse rate of the laser.

The data shows that parallel polarization yields a higher count rate compared to perpendicular polarization. In the saturation regime both polarizations present a count rate that equals the pulse rate. Also, the data for both polarizations reveals an unexpected roll-off of the count rate for powers $N \leq 10^3$.

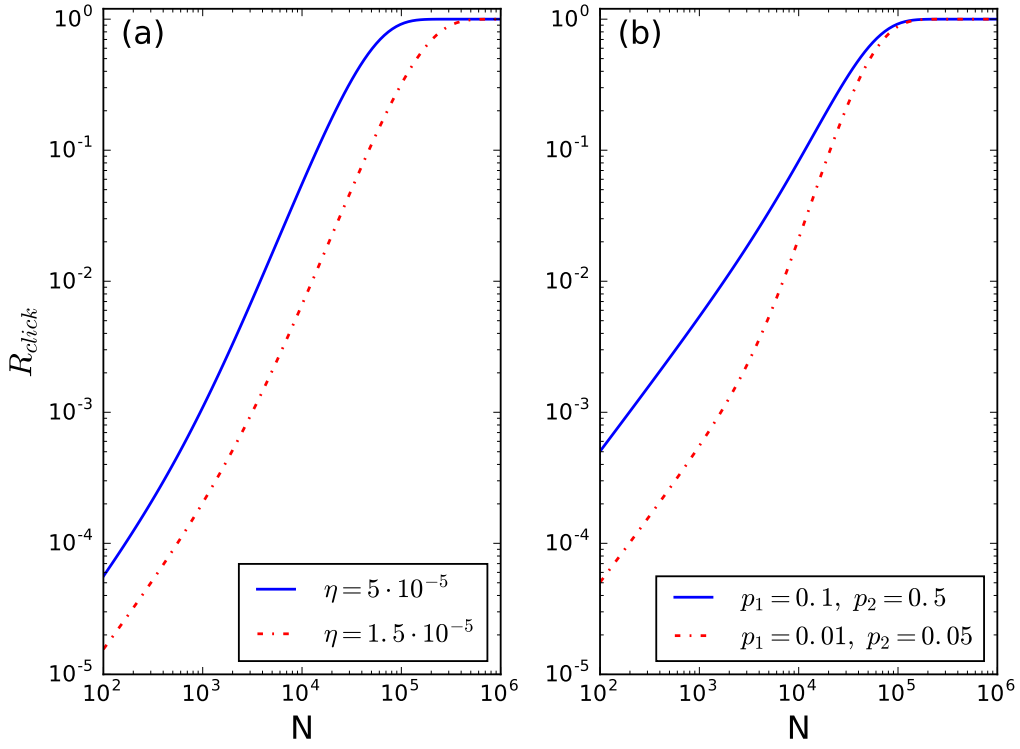

Figure 4.4: *Click probability calculated with equation 4.1. Fig.(a): Click probability with same p_i values ($p_1 = 0.01$, $p_2 = 0.5$, $p_{i>2} = 1$) and different values for η. Both curves present the same shape and lie on top of each other if are shifted. Fig.(b): Click probability for $\eta = 5 \cdot 10^{-5}$ and different p_i values. The red and blue lines show a different shape and it is not possible to overlap them modifying the value of η of one of the curves.*

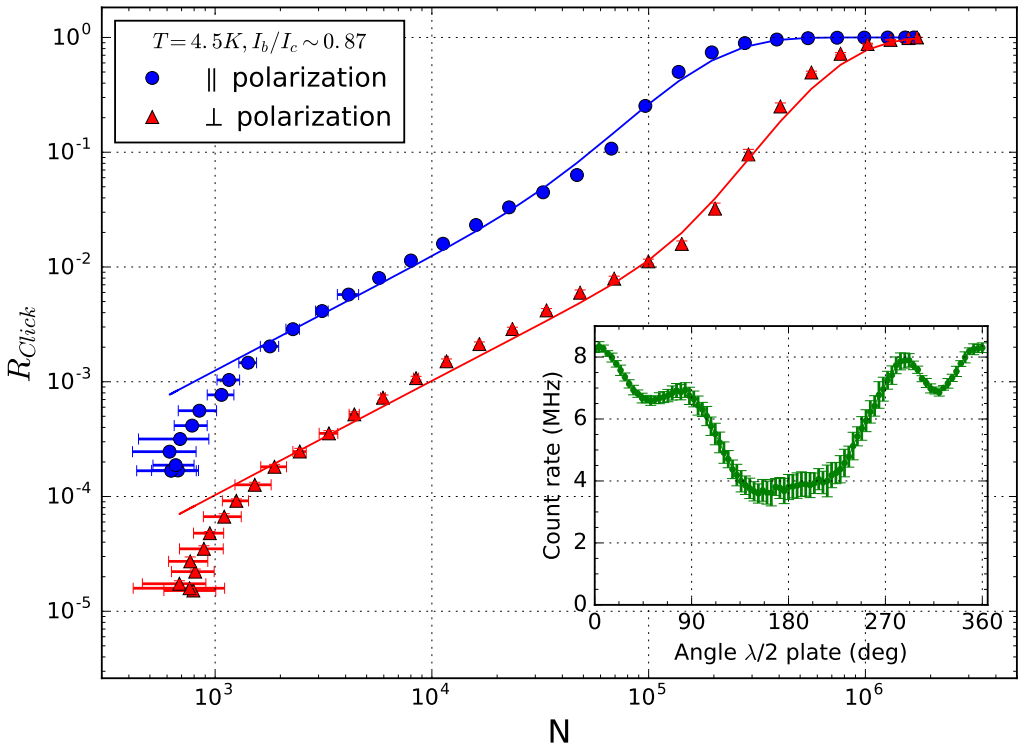

Figure 4.5: *Response of the detector for parallel polarization (blue circles) and perpendicular polarization (red triangles). The blue and red lines correspond to manual fits of the expression 4.1. Inset: Count rate as function of the angle of the second $\lambda/2$ plate (Fig.2.2) at constant power. The results show that the count rate differs by a factor of 2 between $\theta_{\lambda/2} = 0°$ and $\theta_{\lambda/2} = 180°$.*

4.4.3 Discussion.

We attribute the roll-off below $N \sim 10^3$ to the limitation of the power meter used for monitoring the power that cannot measure the lowest powers accurately. The roll-off can be explained by a small background or dark current that we cannot correct for in the current experiment. We do not consider these points when quantifying the response of the detector. The NbN sample is capable of detecting these low powers, and shows that there is room for improvement if a power meter with broader dynamical range is used. Once this problem is fixed, the next limitation will be set by the extinction ratio of the polarizers used, which limits the power range to approximately 5 orders of magnitude.

To quantify the differences between the two responses, manual fits to equation 4.1 are presented by the solid lines. The values for parallel polarization are $\eta_{\parallel} = 1.5 \cdot 10^{-5}$, $p_{\parallel 1} = 0.08$, $p_{\parallel 2} = 0.11$, $p_{\parallel i>2} = 1$ and for perpendicular polarization are $\eta_{\perp} = 5.15 \cdot 10^{-6}$, $p_{\perp 1} = 0.02$, $p_{\perp 2} = 0.03$, $p_{\perp 3} = 0.07$ and $p_{i>3} = 1$. According to this result, the absorption of the nanowire is different to both polarizations as expected because $\eta_{\parallel} \neq \eta_{\perp}$ but also the detection efficiencies are different, $p_{\parallel i} = p_{\perp i}$. Further experiments show that extreme caution must be exercised in the interpretation of these results.

In order to check that the different response in Fig.4.5 is indeed caused by a change of polarization, the count rate as a function of $\theta_{\lambda/2}$ (angle of the second $\lambda/2$ plate) for constant power was measured (inset of Fig.4.5). The count rate for $\theta_{\lambda/2} = 0^{\circ}$ and $\theta_{\lambda/2} = 180^{\circ}$ should be identical. The inset of Fig.4.5 shows a factor 2 difference in the count rate that can be explained by small deviations of the beam while rotating the $\lambda/2$ plate. According to the manufacturer the beam deviation is $\leq 10 arcsec$, which in our experimental set up could lead to a deviation of $\leq 4.8 \mu m$. Considering a gaussian beam, the diameter of the spot on the sample is $\sim 30 \mu m$, producing a shift of the spot on the sample of $\sim 16\%$ of the spot size. This variation of the position of the spot on the sample could lead to a different intensity illuminating the detector and as a consequence a different photon number distribution. If this is the case, the response of the two polarizations could not be directly compared. The probable deviation of the beam caused by the $\lambda/2$ plate would also affect our first $\lambda/2$ plate used to attenuate the power (Fig.2.2). This hypothesis is also consistent with the fact that the response of the detector depends on the experimental method used to optimize the number of counts.

Several methods can be used to reduce the effect of the deviation. Previously a much larger beam size was used to make the setup less sensitive

to alignment errors and vibrations. This leads to undesirable heating effects and excludes the possibility to measure the efficiency of meandering wire detectors directly. An alternative could be to test several waveplates and select those with the smallest wedge. Preliminary results show improvement, but the effect cannot be ignored completely. As a last resort we suggest to measure the detector response as a function of polarization and position using e.g. motorized translation stages to move the beam.

Chapter 5

Conclusions.

We have presented the importance of temperature and bias voltage in the activation and deactivation mechanism of the dark counts as well as in the sensitivity of the detector. Our results present a lack of dark counts in the superconducting state at $T = 7.85 \pm 0.05K$ and the complete deactivation of the dark counts mechanism above $8.05 \pm 0.05K$ for count rates larger than $1Hz$ and amplified voltage pulses larger than $200mV$. A change of regime was found in the $I_c(T)$ dependence at $7.9 \pm 0.1K$, close to the disappearance of the temperature where the dark counts disappear in the superconducting state.

We have successfully introduced a continuous power monitor and isolated mechanical vibrations in the experimental setup. These two improvements will allow an improved accuracy of the measurements. In addition a reduced size of the beam spot is used to strongly reduce the undesired effects caused by local heating.

We have attempted to measure the effect of polarization on the detector response aiming to show directly that both the absorption efficiency and internal detection efficiency are affected by polarization. A strong effect is observed, but the origin of the effect is inconclusive. In addition to the polarization dependence, the position of the pump spot changes the detector response. For the pump spot size and the wedge of the waveplates used we find a 16% deviation in position when rotating the waveplate to change polarization.

Acknowledgements.

I would like to thank Michiel for all the advice, intriguing and fascinating scientific conversations and helping me to do my first steps in research. I really appreciate all the time we spent together in the lab and in front of the whiteboard. I am really grateful for having the opportunity of doing my bachelor project with you. I also want to thank Daan for all the help, advice and teamwork during these months.

Quiero agradecer a mis familiares y amigos, en especial a los que llevo en el camino, todo el apoyo y cariño que siempre me han dado.

Los agradecimientos más especiales lo guardo para el final. Me gustaría agradecer a mi hermano Alejandro que me transmitiese la curiosidad por las matemáticas y la física, por ser uno de mis ejemplos a seguir y ayudarme siempre en todo lo que he necesitado. Por último no puedo más que agradecer a mi padre y a mi madre todo lo que han hecho para convertirme en la mejor persona posible. Esto va desde inculcarme las ganas vivir y aprender, a darme todas las oportunidades para hacerme feliz. Sólo puedo daros las más sinceras gracias a los 3.

References

[1] G. N. Gol'tsman, O. Okunev, G. Chulkova, A. Lipatov, A. Semenov, K. Smirnov, B. Voronov, A. Dzardanov, C. Williams, and R. Sobolewski, *Picosecond superconducting single-photon optical detector*, Applied Physics Letters **79**, 705 (2001).

[2] T. Yamashita, S. Miki, K. Makise, W. Qiu, H. Terai, M. Fujiwara, M. Sasaki, and Z. Wang, *Origin of intrinsic dark count in superconducting nanowire single-photon detectors*, Applied Physics Letters **99**, 161105 (2011).

[3] F. Marsili, V. B. Verma, J. A. Stern, S. Harrington, A. E. Lita, T. Gerrits, I. Vayshenker, B. Baek, M. D. Shaw, R. P. Mirin, and S. W. Nam, *Detecting single infrared photons with 93% system efficiency*, Nature Photonics **7**, 210 (2013).

[4] C. Zinoni, B. Alloing, L. H. Li, F. Marsili, A. Fiore, L. Lunghi, A. Gerardino, Y. B. Vakhtomin, K. V. Smirnov, and G. N. Gol'tsman, *Single-photon experiments at telecommunication wavelengths using nanowire superconducting detectors*, Applied Physics Letters **91**, 031106 (2007).

[5] R. Collins, R. Hadfield, V. Fernandez, S. Nam, and G. Buller, *Low timing jitter detector for gigahertz quantum key distribution*, Electronics Letters **43**, 180 (2007).

[6] D. M. Boroson and B. S. Robinson, *The Lunar Laser Communication Demonstration: NASAâs First Step Toward Very High Data Rate Support of Science and Exploration Missions*, Space Science Reviews **185**, 115 (2014).

[7] N. R. Gemmell, A. McCarthy, B. Liu, M. G. Tanner, S. D. Dorenbos, V. Zwiller, M. S. Patterson, G. S. Buller, B. C. Wilson, and R. H. Had-

field, *Singlet oxygen luminescence detection with a fiber-coupled superconducting nanowire single-photon detector*, Optics Express **21**, 5005 (2013).

[8] A. D. Semenov, G. N. Gol'tsman, and A. A. Korneev, *Quantum detection by current carrying superconducting film*, Physica C: Superconductivity **351**, 349 (2001).

[9] A. Semenov, A. Engel, H.-W. HÃŒbers, K. Il'in, and M. Siegel, *Spectral cut-off in the efficiency of the resistive state formation caused by absorption of a single-photon in current-carrying superconducting nano-strips*, The European Physical Journal B **47**, 495 (2005).

[10] L. N. Bulaevskii, M. J. Graf, and V. G. Kogan, *Vortex-assisted photon counts and their magnetic field dependence in single-photon superconducting detectors*, Physical Review B **85, 014505** (2012).

[11] A. N. Zotova and D. Y. Vodolazov, *Photon detection by current-carrying superconducting film: A time-dependent Ginzburg-Landau approach*, Physical Review B **85, 024509** (2012).

[12] J. J. Renema, Q. Wang, R. Gaudio, I. Komen, K. op t Hoog, D. Sahin, A. Schilling, M. P. van Exter, A. Fiore, A. Engel, and M. J. A. de Dood, *Position-Dependent Local Detection Efficiency in a Nanowire Superconducting Single-Photon Detector*, Nano Letters **15**, 4541 (2015).

[13] V. Anant, A. J. Kerman, E. A. Dauler, J. K. W. Yang, K. M. Rosfjord, and K. K. Berggren, *Optical properties of superconducting nanowire single-photon detectors*, Optics Express **16**, 10750 (2008).

[14] E. F. C. Driessen, F. R. Braakman, E. M. Reiger, S. N. Dorenbos, V. Zwiller, and M. J. A. de Dood, *Impedance model for the polarization-dependent optical absorption of superconducting single-photon detectors*, The European Physical Journal Applied Physics **47**, 10701 (2009).

[15] J. J. Renema, G. Frucci, Z. Zhou, F. Mattioli, A. Gaggero, R. Leoni, M. J. A. de Dood, A. Fiore, and M. P. van Exter, *Modified detector tomography technique applied to a superconducting multiphoton nanodetector*, Optics Express **20**, 2806 (2012).

[16] J. J. Renema, G. Frucci, Z. Zhou, F. Mattioli, A. Gaggero, R. Leoni, M. J. A. de Dood, A. Fiore, and M. P. van Exter, *Universal response curve for nanowire superconducting single-photon detectors*, Physical Review B **87** (2013).

[17] Q. Wang, J. J. Renema, A. Gaggero, F. Mattioli, R. Leoni, M. P. van Exter, and M. J. A. de Dood, *How noise affects quantum detector tomography*, Journal of Applied Physics **118**, 134501 (2015).

[18] J. J. Renema, *The physics of nanowire superconducting single-photon detectors*, PhD thesis, Leiden University, 2015.

[19] A. J. Kerman, E. A. Dauler, W. E. Keicher, J. K. W. Yang, K. K. Berggren, G. Gol'tsman, and B. Voronov, *Kinetic-inductance-limited reset time of superconducting nanowire photon counters*, Applied Physics Letters **88**, 111116 (2006).

[20] J. Tyan and J. T. Lue, *Grain boundary scattering in the normal state resistivity of superconducting NbN thin films*, Journal of Applied Physics **75**, 325 (1994).

[21] A. Nigro, G. Nobile, M. G. Rubino, and R. Vaglio, *Electrical resistivity of polycrystalline niobium nitride films*, Physical Review B **37**, 3970 (1988).

[22] Z. Z. Zhou, *Multi-photon detection with superconducting nanowires*, PhD thesis, Technische Universiteit Eindhoven, 2014.

[23] J. Kitaygorsky, I. Komissarov, A. Jukna, D. Pan, O. Minaeva, N. Kaurova, A. Divochiy, A. Korneev, M. Tarkhov, B. Voronov, I. Milostnaya, G. Gol'tsman, and R. Sobolewski, *Dark Counts in Nanostructured NbN Superconducting Single-Photon Detectors and Bridges*, IEEE Transactions on Applied Superconductivity **17**, 275 (2007).

[24] A. Engel, A. Semenov, H.-W. HÃŒbers, K. Ilâin, and M. Siegel, *Fluctuation effects in superconducting nanostrips*, Physica C: Superconductivity and its Applications **444**, 12 (2006).

[25] J. S. Lundeen, A. Feito, H. Coldenstrodt-Ronge, K. L. Pregnell, C. Silberhorn, T. C. Ralph, J. Eisert, M. B. Plenio, and I. A. Walmsley, *Tomography of quantum detectors*, Nature Physics **5**, 27 (2009).